Catalysis Today 334 (2019) 223–230

Contents lists available at ScienceDirect

Catalysis Today

journal homepage: www.elsevier.com/locate/cattod

Insights into the activation of silica-supported metallocene olefin polymerization catalysts by methylaluminoxane

Marjolein E.Z. Velthoen, Jelle M. Boereboom, Rosa E. Bulo, Bert M. Weckhuysen*

Inorganic Chemistry and Catalysis Group, Debye Institute for Nanomaterials Science, Utrecht University, Universiteitsweg 99, 3584 CG Utrecht, the Netherlands

ARTICLE INFO

Keywords:
Metallocenes
Methylaluminoxane
Olefin polymerization
Activation
UV–vis DR spectroscopy
TD-DFT

ABSTRACT

Metallocene-based olefin polymerization catalysts often require large excesses of co-catalyst for optimal catalyst activation. In this work, mechanistic insights into the activation of supported metallocenes by methylaluminoxane as co-catalyst are acquired. UV–vis diffuse reflectance (DR) spectroscopy of five metallocene catalysts with varying co-catalyst loading reveals the presence of different metallocene species on the surface of the catalyst particles. Deconvolution of the obtained spectra, in combination with an extensive TD–DFT study of UV–vis DR spectra of metallocene structures results in a proposed activation mechanism. We find that with increasing MAO loading, more $AlMe_2^+$-bound metallocenes are observed with a shift towards the trimethylaluminum-stabilized cationic methylated metallocene compound. This shift can be directly correlated with a higher activity in the olefin polymerization reaction. Based on this finding, we propose a universal metallocene activation mechanism in which the cationic methylated metallocene is the active species. This species is formed through initial interaction with $AlMe_2^+$, followed by ligand exchange with MAO and stabilized in complex with trimethylaluminum as a dormant species.

1. Introduction

After the discovery of Phillips [1–4] and Ziegler–Natta catalysis [5–8], a major breakthrough in polymer production was the invention of the single-site metallocene catalyst in combination with methylaluminoxane (MAO), produced through controlled hydrolysis of trimethylaluminum (TMA), as a co-catalyst for olefin polymerization [9–12]. In particular, the possibility to tailor the electronic and steric environment of the catalytic complex by ligand modification, thereby directly influencing the catalytic performance, as well as the resulting polymer properties, has been the motivation for a wide-spread search for new catalysts of this type [13–17]. Heterogenization of these single-site catalysts brings along the anticipated synergy between homogeneous and heterogeneous catalysis: while retaining their single-site characteristics such as narrow molecular weight distributions and stereoselectivity, the heterogenized catalysts can be employed in gas- and slurry-phase processes (drop-in technology) and produce morphologically more uniform polymer particles preventing reactor fouling [10,18–20].

Single-site catalysts are typically sandwich complexes composed of a group 4 transition metal and cyclopentadienyl-derived ligands. The required activation of these complexes prior to catalytic reaction, proceeds through the interaction with the aluminum alkyl (MAO) co-catalyst giving rise to the $[L_nMMe]^+[MAO]-$ ion pair as active metallocene species [21,22]. Exact mechanisms describing this activation of metallocenes through the interaction with MAO, however, have not been irrefutably proven. This is not in the least due to a still limited knowledge on the responsible active component in the MAO co-catalyst despite extensive theoretical and experimental studies on its chemical structure [23,24]. Recently, Linnolahti and co-workers reported that MAO favors cage-like structures with four-coordinate Al and three-coordinate O, stabilized with associated TMA on the edges and corresponds to the general molecular formula $(MeAlO)_n(Me_3Al)_m$ [25]. These TMA-associated sites containing five-coordinate bridging methyl groups are reactive and give the MAO its function as metallocene activator. For some sites, this reactivity relies on their possession of latent Lewis acidity: upon ligand abstraction from the metallocene precursor, the Al-C bridging bond can break. Other TMA-associated sites can be ionized through $AlMe_2^+$ cleavage, leaving an anionic TMA-bound three-coordinate O. Both sites are abundant in MAO solutions and both are responsible for co-catalytic properties of MAO [25–31].

Interaction with either these Lewis acid sites or $AlMe_2^+$ species with the dichloride metallocene precursor $[L_2ZrCl_2]$ leads to the extraction of the chloride ligands and the methylation of the zirconium center $[L_2ZrMe]^+$ [32]. The cationic metallocene is then stabilized in a complex with an MAO–Cl– species [33]. The Al/Zr ratio was found to

* Corresponding author.
E-mail address: B.M.Weckhuysen@uu.nl (B.M. Weckhuysen).

https://doi.org/10.1016/j.cattod.2018.11.019
Received 1 July 2018; Received in revised form 21 October 2018; Accepted 7 November 2018
Available online 13 November 2018

strongly determine which mechanism prevails [27,34–36]. Deffieux and co-workers investigated a metallocene catalyst in solvents with different polarity at different MAO concentrations with UV–vis spectroscopy [37–40]. They observed an absorption band associated with a "ligand to metal charge transfer", hypsochromically shifting upon the addition of MAO. They ascribed this to the mono–methylation of the metallocene dichloride precursor. Conversely, at very high MAO concentrations, the band was observed to bathochromically shift, which the authors ascribed to the abstraction of the second chloride ligand. These band assignments, however, were not rationalized with calculations or other experimental characterization. Instead, the interpretation of the bands was merely intuitively reasoned based on the Lewis acid assisted mechanism and the role of $AlMe_2^+$ was not considered. Recent electrospray-ionization mass spectrometric studies of MAO, however, demonstrated that alkylation and ionization are separate events that occur at competitive rates depending on the solvent polarity [36,41]. This indicates that metallocene activation mechanistically depends on the environment.

It is important to note that studies on the structural characterization of MAO and its role in the metallocene activation are mostly either quantum chemical calculations or experimental studies on the catalytic system in solution. The rational design and subsequent preparation of active and selective supported metallocene catalysts, on the other hand, is a complex process. Numerous synthesis parameters, such as metallocene structure, co-catalyst loading, impregnation conditions, and choice of support were found to strongly influence the catalyst structure and corresponding catalytic performance on both the bulk and single particle level [42–47]. Recently, we have reported the influence of the MAO co-catalyst loading on the activity of the heterogenized metallocene catalyst in the olefin co-polymerization reaction [48]. A set of silica-supported MAO/Metallocene olefin polymerization catalysts was prepared in which only the loading of the MAO co-catalyst was varied, as illustrated in Scheme 1. It was found that a minimum amount of MAO (12 wt% Al in the solid activator) is necessary to quench remaining silanol groups, responsible for metallocene deactivation, on the solid activator surface. Furthermore, a higher MAO loading led to an increase in the amount of weak Lewis acid sites, which were linearly correlated with the olefin polymerization activity of the final catalyst. These weak Lewis acid sites are the origin of mobile $AlMe_2^+$ groups, directly responsible for metallocene activation [25,31]. In contrast, the stronger Lewis acid sites were found less abundant in the solid activators and uncorrelated with the MAO loading. This suggests that the $AlMe_2^+$-assisted metallocene activation prevails over the Lewis acid-assisted mechanism in the supported metallocene catalyst.

In this work we continue our investigation into the influence of the MAO co-catalyst loading on the activity of the metallocene catalyst in the olefin polymerization reaction. Scheme 1 illustrates the stepwise preparation of the series of metallocene catalysts under study and the approach of the current study. An extensive combined UV–vis DRS/TD-DFT study is employed to elucidate the observed changes in catalytic performance as a function of MAO loading. UV–vis DR spectroscopy reveals the presence of different metallocene species on the catalyst surface and TD-DFT aids the interpretation of these results. Finally, a mechanism is proposed based on the results in this work, that describes the activation of metallocenes through the interaction with $AlMe_2^+$ species that are inherent to the MAO co-catalyst.

2. Experimental and computational details

2.1. Sample preparation

The preparation of the materials was done as described in previous

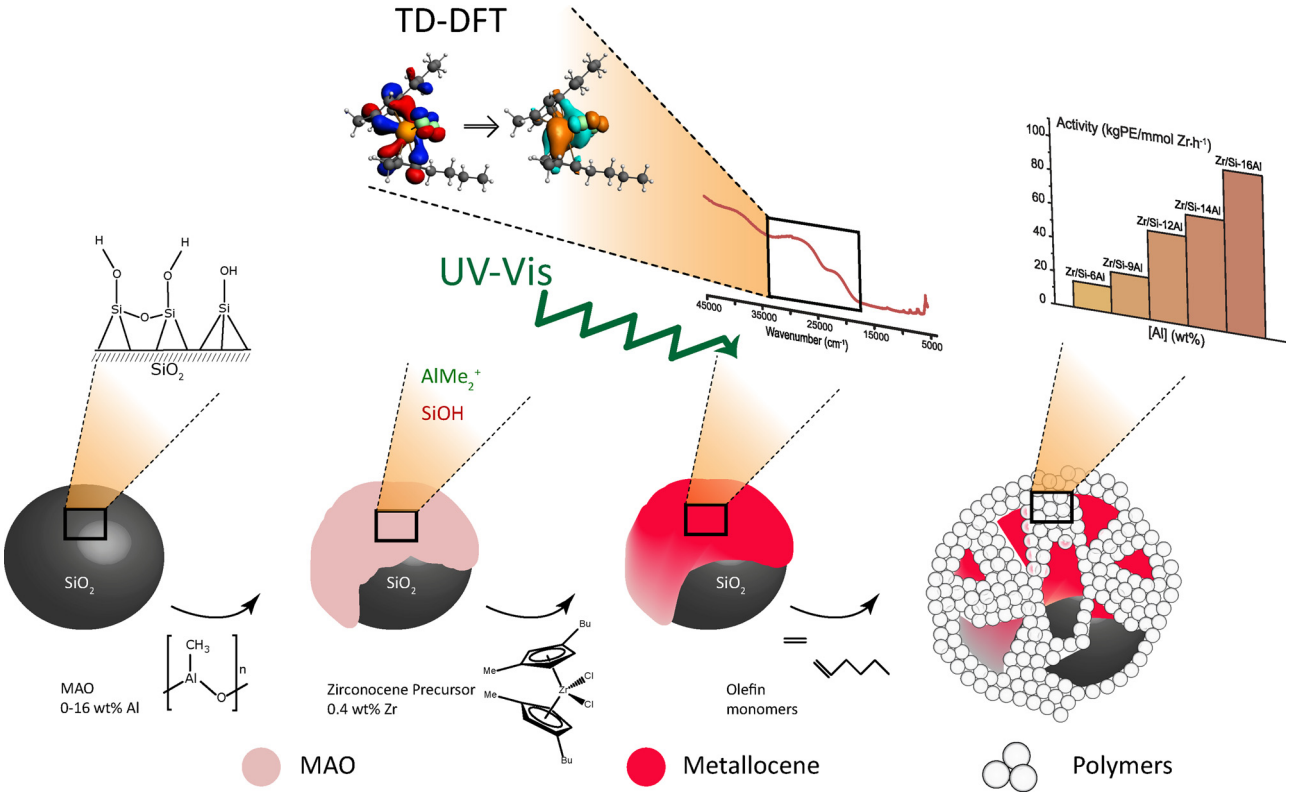

Scheme 1. Schematic of the stepwise preparation of the set of metallocene-based olefin polymerization catalysts under study. The silica support is impregnated with different loadings of MAO (solid activators), while the zirconocene precursor loading is kept constant, resulting in five catalysts with a varying co-catalyst loading. With increasing MAO loading, the amount of deactivating Si−OH groups decreases, while the amount of metallocene-activating $AlMe_2^+$ species increases. As a result, the olefin polymerization activity increases linearly with increasing MAO loading [48]. In this work, we investigate the presence of different metallocene species in the five catalysts as a function of the MAO loading with UV–vis diffuse reflectance spectroscopy. The results are rationalized by TD-DFT calculations.

work from our group: [48] Catalysts were prepared according to a synthetic protocol comprising three steps: silica treatment, MAO anchoring, and zirconocene deposition. All steps were carried out under N_2 atmosphere and all solvents utilized for the synthesis were analytical grade and treated prior to any use in synthesis: Toluene (Fischer Chemical, purity: > 99.99%) was degassed through dry nitrogen bubbling and dried employing molecular sieves. N-pentane (Fischer Chemical, purity: 99%) was dried over calcium hydride. The moisture content was measured by Karl-Fischer titration, giving a content level less or equal to 2 ppm. The 30% MAO solution containing approximately 26.2 wt% MAO and 5.2 wt% TMA was stored in a fridge at 255 K in order to prevent gel formation. Reference material $ZrCl_4$ (Sigma-Aldrich: purity > 99.9%) was used as received. All synthetic steps were carried out using standard glovebox techniques and the prepared samples were stored in a N_2 glovebox, inside dark and well-sealed containers. The syntheses yielded a set of catalysts, consisting of the parent silica, increasing MAO loading, and constant metallocene loading, denoted Zr/Si-*n*Al. In this notation, *n* indicates the weight loading of Al, with 0 wt% being the lowest and 16 wt% being the highest loading.

A commercial amorphous silica (ES767 from PQ), with a surface area of 276 m^2/g, a pore volume of 1.56 cm^3/g, an average pore width of 19.2 nm and a mean particle size of approximately 33 µm diameter, was heated at 423 K for 5 h on a fluidized bed under a dry N_2 flow to remove moisture. In a glass round-bottom flask, an MAO solution was slowly added to a silica/toluene slurry (respective weight ratio of 1:5) under gentle mechanical agitation (precursor: Albemarle 30% MAO solution: 26.2 wt% in toluene, 5.2 wt% residual TMA). Subsequently, the whole mixture was heated at toluene reflux temperature (ca. 384 K) for several hours. The solid was filtered on a frit, washed three times with dry n-pentane followed by a drying treatment under vacuum for 1 h at room temperature. Next, a determined quantity of the metallocene precursor (bis(1-methyl-3-butylcyclopentadienyl) zirconium dichloride) to reach the targeted zirconium content of 0.4 wt% was added to a slurry of the prepared MAO/SiO_2 solid activators in toluene (respective weight ratio of 1:5) in a glass round bottom ask. The colored slurry was then mechanically stirred for several hours at room temperature. The final supernatant was colorless, indicating that most of the metallocene was anchored to the supported MAO co-catalyst.

2.2. Sample characterization

UV–vis diffuse reflectance spectroscopy was performed in reflectance mode using a CRAIC 20/30 PVTM micro-spectrophotometer equipped with a 15 × 0.28 NA reflective lens. Samples were pressed into self-supported wafers in the glovebox to keep the reflective properties of all samples similar. Samples were then transported under N_2 atmosphere in a well-sealed cell with a quartz lid, and were illuminated with a 30 W halogen lamp. The UV–vis DR spectra were collected in reflectance mode from a spot on top of the wafer surface of approximately 82 × 82 µm and spectra were recorded at different spots of the wafer to ensure reproducibility. A teflon white standard was first measured and automatically subtracted from the UV–vis diffuse reflectance spectra using the Lamdafire spectroscopy software. Deconvolution of the spectra in the energy range 35,000 – 12,500 cm^{-1} was performed by manually choosing a set of Gaussians based on the computed UV–vis spectra and fitting these Gaussians to the experimental spectra using the program Fityk [49]. Based on the first estimates, a set of Gaussians with fixed peak positions was selected to fit all spectra. Only one peak around 35,000 cm^{-1} was allowed to vary, since multiple metallocene species can contribute to absorption in this energy range.

Electron paramagnetic resonance (EPR) spectra were recorded on a Bruker EMX Plus 6000 G instrument with an ER 041 XG X-Band Microwave Bridge. Measurements were performed in a J-Young quartz tube (diameter 5 mm) at 100 K. The reported g-values are calibrated for the magnetic field offset using a reference spectrum of BDPA (g = 2.0036).

2.3. Computational details

All geometry optimizations were performed with the ADF program package [50,51], using the range-separated hybrid functional CAMY-B3LYP [52,53] and a TZP basis set [54]. In order to simulate the theoretical UV–vis spectra of these compounds, the lowest *n* allowed vertical excitations were calculated (n = 20–50) with TD-DFT in ADF [55]. CAMY-B3LYP was chosen because it is provides an accurate description of excitation energies (especially for excitations with large charge transfer character) [56]. Nevertheless, the vertical excitation energies were scaled by a factor of 1.07 to correct for the energy-dependent systematic errors of the TD-DFT functional. In order to compare between the calculated theoretical spectra and the experimental spectra, the simulated peaks were broadened with a Gaussian profile with a half width of 2000 cm^{-1} using the ADF software [50]. The convolution of these simulated bands resulted in a simulated UV–vis spectrum, where the position of the expected most intense absorption band in the UV–vis region for each metallocene can be determined.

3. Results and discussion

Five supported metallocene catalysts in which the only variable parameter is the co-catalyst loading were prepared for this study. Recently, we reported that these five catalysts are all active in the ethylene–1-hexene olefin co-polymerization reaction, but an increase in MAO loading is directly correlated with an increase in activity [48]. This was correlated with only partial metallocene activation or even metallocene deactivation at low MAO loadings. To investigate the presence of different metallocene species on the catalyst and obtain insights in the prevailing activation mechanism on the supported metallocene olefin polymerization catalyst, the catalysts were studied with UV–vis diffuse reflectance spectroscopy. Fig. 1 presents the recorded UV–vis DR spectra (40,000 – 12,500 cm^{-1}) for the five catalysts with increasing co-catalyst (MAO) loading. The silica support does not absorb photons in the UV–vis region and MAO is characterized with a band at 35,700 cm^{-1}, ascribed to charge transfer excitations from the oxygen lone pairs into the empty aluminum orbitals [57]. Figure S1 in the Supporting Information shows the UV–vis DR spectra of the

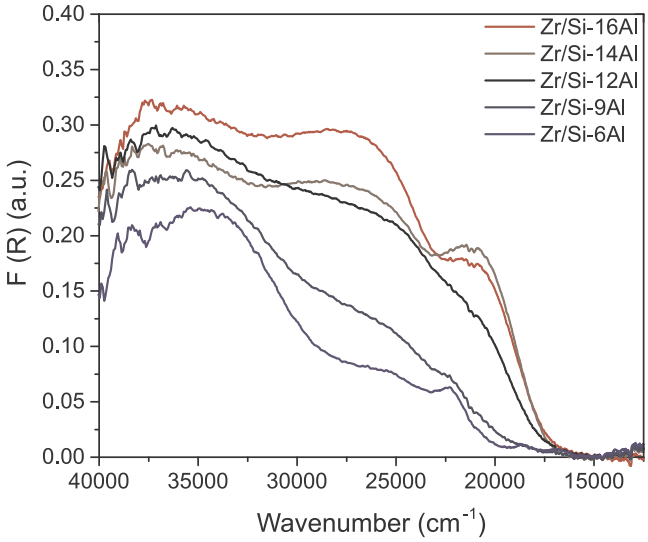

Fig. 1. UV–vis diffuse reflectance spectra recorded for the five catalysts under study with increasing co-catalyst (MAO) loading: Zr/Si-6Al (blue), Zr/Si-9Al (marine), Zr/Si-12Al (black), Zr/Si-14Al (brown), and Zr/Si-16Al (red). (For interpretation of the references to colour in this figure legend, the reader is referred to the web version of this article.)

corresponding solid activators (SiO_2/MAO), indeed demonstrating the presence of merely one absorption band at 35,700 cm^{-1}. All other bands observed in Fig. 1 must, therefore, be attributed to electronic transitions within the metallocenes present in the catalysts.

Closer inspection of the UV–vis DR spectra of the five catalysts reveals three broad absorption regions around 37000, 27,000, and 21,000 cm^{-1}. The first absorption band was ascribed to the presence of MAO in the catalysts. The latter two absorption bands undergo significant shifts upon increasing MAO loading, but their behavior is opposite. The band around 27,000 cm^{-1} shows a hypsochromic shift upon increasing the MAO loading, whereas the band at 21,000 cm^{-1} shifts bathochromically. For the lowest loaded catalysts (Zr/Si-6Al and, to a lesser extent, Zr/Si-9Al) two additional low-intensity bands at 18,000 and 16,850 cm^{-1} are observed.

The interpretation of these UV–vis DR spectra is hampered by the lack of literature on the electronic properties of the heterogenized metallocene-based olefin polymerization catalyst. Apart from the UV–vis spectroscopy studies on the metallocene catalyst in solution by Deffieux and co-workers, as discussed in the Introduction, this catalytic system has not often been studied with UV–vis spectroscopy and if they were, the interpretation of bands was inconclusive [37–40]. In this work, to support and rationalize the interpretation of our UV–vis DR spectra, we have assembled a library of potentially present metallocene structures. For each library structure, we calculated the vertical excitation energy using TD-DFT. These energies were broadened with a Gaussian profile with a half width of 2000 cm^{-1}. The convolution of these simulated absorption bands resulted in a simulated UV–vis spectrum, where the position of the expected most intense absorption band in the UV–vis region can be determined. Fig. 2 shows the vertical excitations, subsequent simulated spectrum and most intense absorption band positions for three example metallocene structures. Furthermore, the charge transfer excitations that mainly contribute to these absorption bands are presented, showing the involved orbitals of the metallocene. Following this procedure, a library of metallocene structures was compiled, as depicted in Figure S2 in the Supporting Information. For each structure, the resulting band position of the lowest energy absorption is indicated. All library structures show multiple absorption bands at energies higher than 35,000 cm^{-1}, classified as high energy transfers. This means that the metallocene structures cannot be differentiated by their spectral features above 35,000 cm^{-1} due to band overlap.

Fig. 3 shows a selection of the most relevant metallocenes as discussed in this work and their corresponding simulated UV–vis spectra with resulting absorption energies. Structure **1** is the metallocene dichloride precursor that was employed in the synthesis of the catalysts. All other structures proposed in this work are derived from proposed activation and deactivation mechanisms in literature. The Lewis acid site (LAS)-assisted metallocene activation pathway is in parallel with the proposed mechanism by Deffieux and co-workers in their UV–vis study of the metallocene catalyst in solution and involves structures **1**-**3** [37–40]. Deactivation of structure **1** through the interaction with silanol groups is represented by the possible formation of structures **4** or **5** [11,48,58]. The $AlMe_2^+$-assisted activation mechanism that results in the active structure **3** stabilized with TMA (structure **8**) is represented with structures **6**-**8** [25,31,36,48].

In order to get more specific information on band positions and

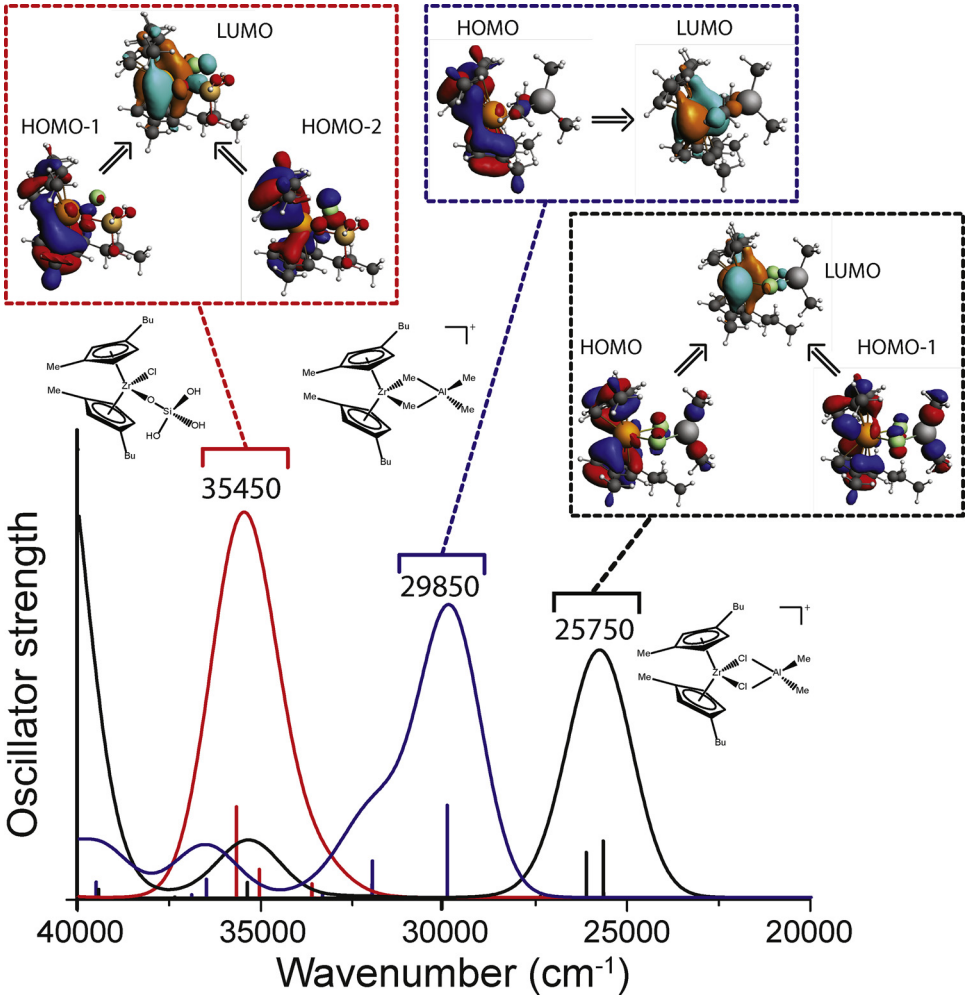

Fig. 2. Vertical excitation energies were calculated with TD-DFT for different metallocenes. These energies are broadened with a Gaussian profile with a half width of 2000 cm^{-1} to yield a simulated UV–vis spectrum. These simulated spectra were employed to determine the expected position of absorption bands in the UV–vis region for each library metallocene. The main contributing charge transfers for each ab including the involved orbitals, are depicted as well. Only charge transfers with orbital strengths larger than 0.01 a.u. are visualized. Black (Structure 6) mainly consists of two excitations: HOMO → LUMO (> 90% orbital character) at 23,885 cm^{-1} with oscillator strength (OS) 0.016 a.u. and HOMO-1 → LUMO (> 80% orbital character) at 24,323 cm^{-1} with OS 0.011 a.u. Blue (Structure 8) mainly consists of one excitation: HOMO → LUMO (almost 95% orbital character) at 27,888 cm^{-1} with OS 0.030. Red (Structure 4) mainly consists of two excitations: One at 32,711 cm^{-1} with OS 0.011 a.u. comprising 55% orbital character HOMO-1 → LUMO and 40% orbital character HOMO-2 → LUMO and one at 33,294 cm^{-1} with OS 0.030 a.u. comprising 40% orbital character HOMO-1 → LUMO and 55% orbital character HOMO-2 → LUMO. (For interpretation of the references to colour in this figure legend, the reader is referred to the web version of this article.)

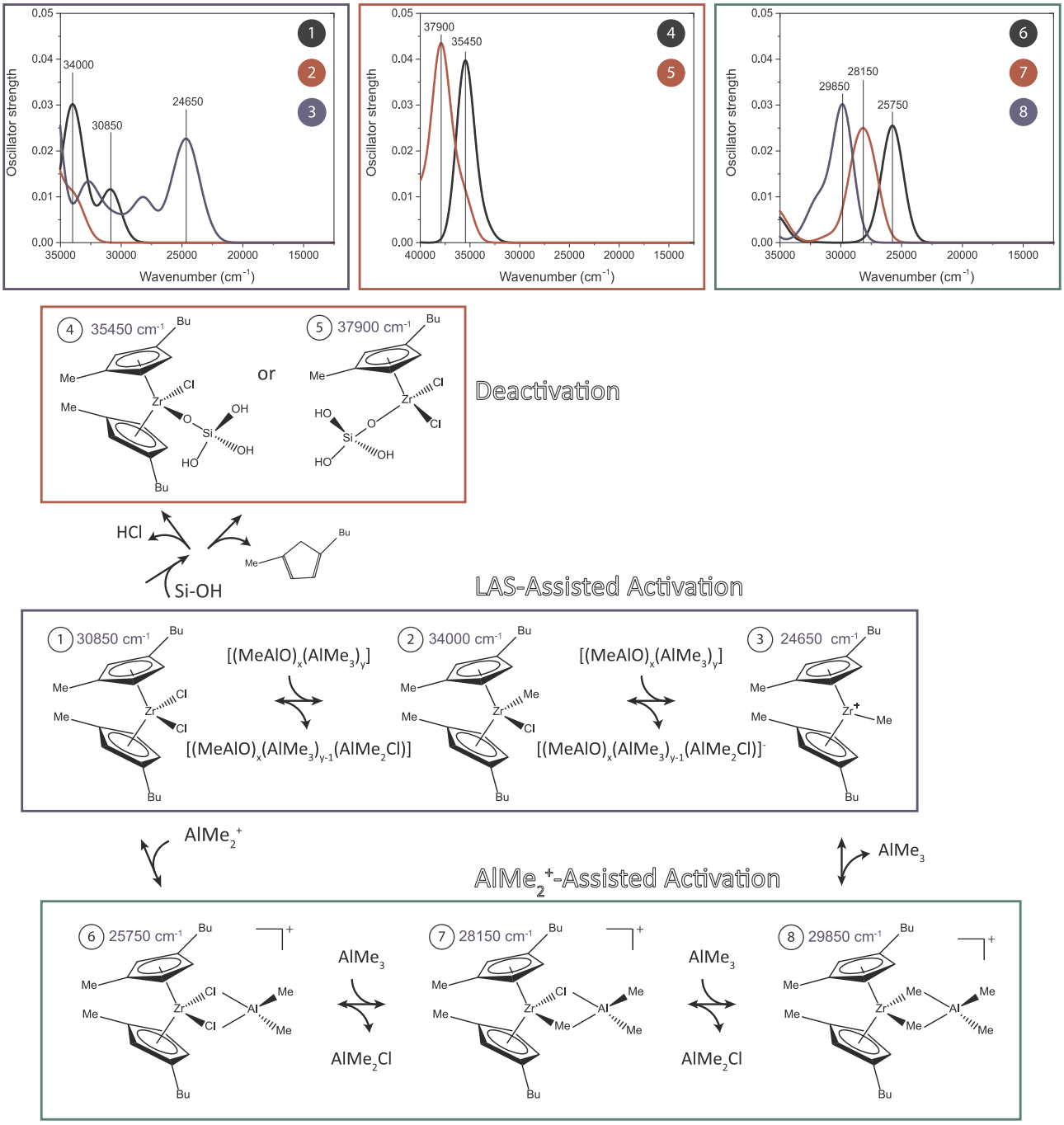

Fig. 3. Selection from the library of metallocenes in Figure S2 based on activation and deactivation mechanisms by MAO proposed in literature and their corresponding simulated UV–vis spectra. For each metallocene structure, the position of the first intense absorption band in the simulated UV–vis spectrum is indicated. Structures 1–3 (blue) represent the Lewis acid site (LAS) assisted activation pathway for the dichloride precursor (structure 1). Structures 4–5 (red) represent two possible deactivation pathways through the interaction with silanol groups on the silica support. Finally, structures 6–8 show the $AlMe_2^+$-assisted activation mechanism of the dichloride precursor (structure 1). (For interpretation of the references to colour in this figure legend, the reader is referred to the web version of this article.)

intensity ratios from the broad and seemingly convoluted bands in the experimental UV–vis DR spectra, each spectrum was deconvoluted with a set of Gaussian curves with fixed band positions. The band positions obtained via the simulated spectra for all library metallocene structures were taken as starting points. As such, we have attempted to deconvolute the experimental spectra employing different combinations of metallocene structures from the library. Fig. 4 shows the only successful way to deconvolute the experimental UV–vis DR spectra and Table 1 provides the resulting integrated band areas of the deconvoluted bands, indicating their contribution to the final spectrum.

Fig. 4 demonstrates that all spectra contain a band at 25,750 cm^{-1}, ascribed to structure **6**. At high MAO loadings (12 wt% Al and higher), a second band emerges and increases in intensity at 29,850 cm^{-1}, ascribed to structure **8**, causing the previously observed general hypsochromic shift of the absorption around 27,000 cm^{-1}. Structure **8** is the dormant species of the active cationic structure **3** and is formed from structure **6** via the $AlMe_2^+$-assisted activation pathway, as indicated in Fig. 3. Structure **7**, being a possible intermediate structure in this mechanism was not observed in the UV–vis DR spectra. The increasing presence of structure **6** (as indicated in Table 1) with increasing MAO

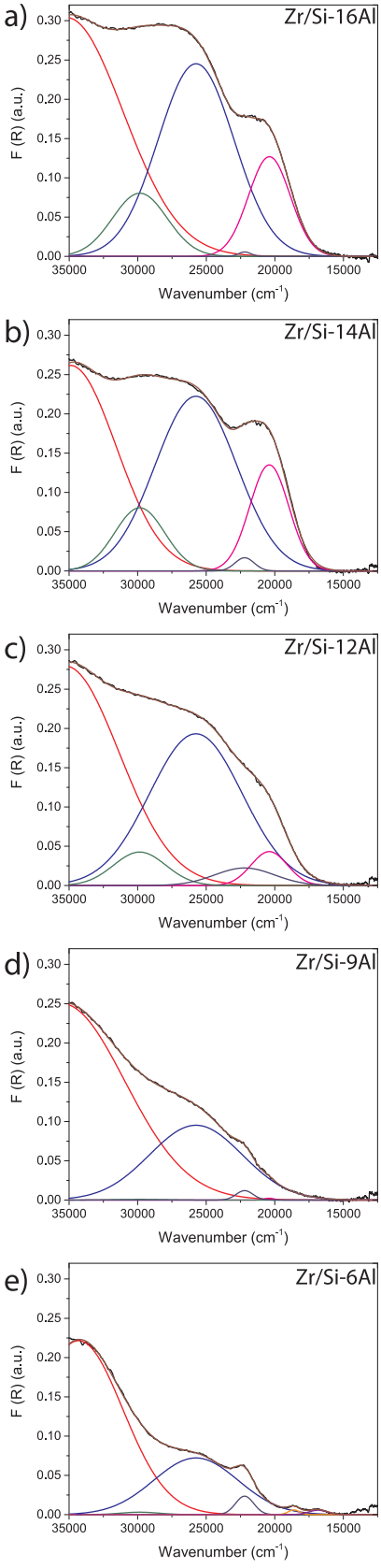

Fig. 4. Deconvolution of the UV–vis spectra for catalysts Zr/Si-16Al (a), Zr/Si-14Al (b), Zr/Si-12Al (c), Zr/Si-9Al (d), and Zr/Si-6Al (e), using a fixed set of Gaussian profiles at 29,850 cm^{-1} (green), 25,750 cm^{-1} (blue), 22,350 cm^{-1} (marine), 20,400 cm^{-1} (magenta), 18,600 cm^{-1} (orange), and 16,850 cm^{-1} (purple). Only one Gaussian (red) was allowed to vary in position and the fit of the spectra using these Gaussians is also indicated (wine). (For interpretation of the references to colour in this figure legend, the reader is referred to the web version of this article.)

loading can be directly correlated with a previously reported increase in $AlMe_2^+$ species in the co-catalyst [48]. The formation of structure **8** appears to only happen at high concentrations of structure **6**, suggesting a chemical equilibrium between the two with the equilibrium position being far to the left. We propose that upon olefin insertion, TMA is released from structure **8**, forming the active metallocene species bound to the first olefin monomer. Furthermore, we propose that this means that the actual cationic structure **3** is never present in the supported metallocene catalyst.

It is important to note that the absence of structures **1–5** cannot be indisputably established. Especially in the catalysts with a low amount of co-catalyst (Zr/Si-6Al and Zr/Si-9Al), the presence of deactivated metallocene structures is highly probable. In the Supporting Information, Figures S2 and S3 show the influence of losing more than one ligand on the UV–vis spectrum as well (Structures **12-14**). Such structures do not absorb light in the 35,000 – 12,500 cm^{-1} range. This means that the deactivation mechanism simply cannot be observed with UV–vis diffuse reflectance spectroscopy. Besides, the activation pathway from structure **1** to structure **3** is catalyzed by strong Lewis acid sites [29]. Our previous work indicated that strong Lewis acid sites are present in all solid activators. In contrast with $AlMe_2^+$ species, however, their abundance was low and uncorrelated with the MAO loading. Possibly, a few metallocene structures are activated through this pathway. The strong differences in catalytic activity for the five catalysts under study, however, can only be explained by the $AlMe_2^+$ concentration in the solid activators and the shifting equilibrium between structures **6** and **8**. Therefore, the $AlMe_2^+$-assisted activation mechanism prevails in the heterogenized metallocene-based olefin polymerization catalyst.

A question that remains is which metallocene structures are the origin of the absorption bands below 25,000 cm^{-1}. In this lower energy range, deconvolution revealed that the band around 21,000 cm^{-1} consists of two bands at 22,350 and 20,400 cm^{-1} with different intensity ratios depending on the MAO loading. Table 1 indicates that at low MAO loading, the absorption band at 22,350 cm^{-1} prevails, while with increasing loading, the 20,400 cm^{-1} appears. To the best of our knowledge, absorption bands below 25,000 cm^{-1} have never been reported for the metallocene olefin polymerization catalyst and might, therefore, correspond to metallocene structures that only exist in the heterogenized catalyst.

Zirconium d-d transitions are highly implausible, since the metal center has a 4+ oxidation state, resulting in empty d-orbitals. Lower oxidation states for zirconium in metallocenes, precursor or activated, are rarely reported. To verify the absence of Zr(III) (d1) species, X-Band EPR spectroscopy was employed. It must be noted that Zr(III) species are generally difficult to detect with EPR spectroscopy, especially under the currently employed experimental conditions [59]. In order to unambiguously detect Zr(III) species, additional XPS or XANES experiments could be performed. The resulting spectra (Figure S3 in the Supporting Information), however, do not contain any EPR peaks related to the presence of Zr(III) (d1) species. Therefore, based on our experimental results, we have excluded d-d transitions from the UV–vis spectral analysis.

Possibly, a monomeric metallocene species does not absorb light at these energies, but a polymeric structure can. To explore this option, we have modelled the dimeric species of structures **1–3** and **8** and modelled their UV–vis spectrum. Dimeric metallocenes were shown to be unstable, so we do not expect to find these in our catalysts [36]. These calculations, therefore, mainly served the purpose of demonstrating the

Table 1
Integrated band areas for the deconvoluted bands of the UV–vis DR spectra for each catalyst. The color coding corresponds to the deconvoluted spectra in Fig. 4.

Catalyst	29,850 cm^{-1}	25,750 cm^{-1}	22,350 cm^{-1}	20,400 cm^{-1}	18,000 cm^{-1}	16,850 cm^{-1}
Zr/Si-16Al	401	1699	6	486	0	0
Zr/Si-14Al	367	1659	29	484	0	0
Zr/Si-12Al	204	1635	121	143	0	0
Zr/Si-9Al	4	806	19	2	0	0
Zr/Si-6Al	11	556	39	0	6	10

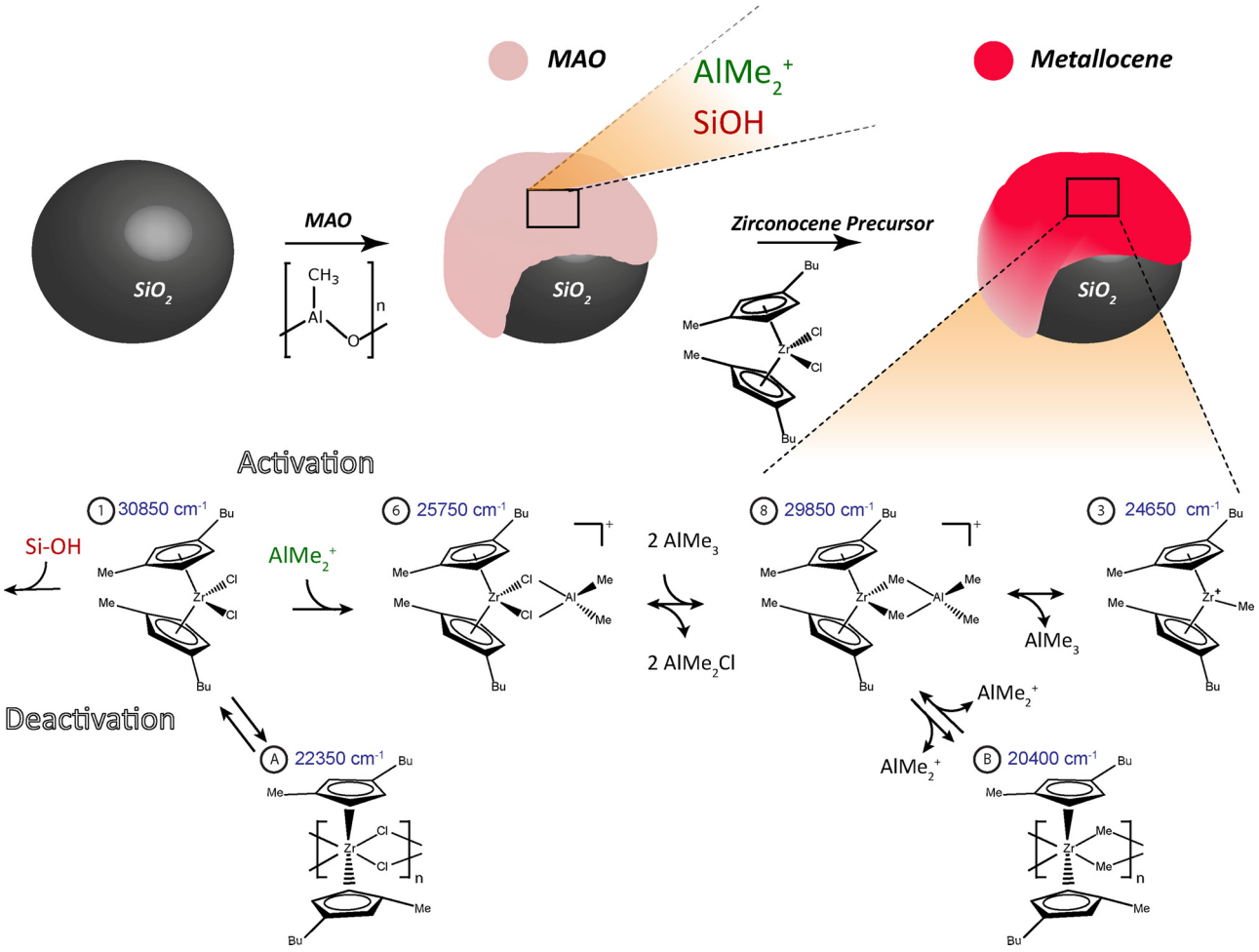

Scheme 2. Schematic of the main conclusions from this work. A metallocene precursor can either be deactivated by silanol groups, activated by $AlMe_2^+$ groups, or adopt a resting state polymeric form. Activation with $AlMe_2^+$ groups leads to formation of structure 6, followed by the formation of structure 8 through ligand exchange with the MAO. Structure 8 is a dormant species for the active species structure 3. Upon formation, however, structure 3 is not stable on the catalyst surface and adopts a polymeric form.

influence of forming larger metallocene species on the resulting UV–vis spectrum. The dimeric structures (**9–11** and **16**) and their simulated UV–vis spectra can be found in Figure S4 in the Supporting Information and absorb light at 24750, 25700, 25700, and 24,650 cm^{-1}, respectively, which are significant shifts in comparison with their monomeric variants, but they do not reach the 21,000 cm^{-1} yet. Extrapolating this shift in the UV–vis spectrum from the monomeric to the dimeric metallocene, we suggest the formation of a type of polymeric (n > 2) metallocene in the heterogenized catalytic system.

To investigate this further, we prepared a reference catalyst without MAO (Zr/Si-0Al), for which the UV–vis spectrum and deconvolution is shown in Figure S5 in the Supporting Information. Charge transfers in polymeric metallocenes are difficult to model with TD-DFT, so for the interpretation of the band around 21,000 cm^{-1} we have to base our spectral interpretation on the experimental UV–vis DRS evidence from reference samples Zr/Si-0Al and $ZrCl_4$. First, the electronic spectrum for reference sample Zr/Si-0Al indicates three distinctive bands at 22,350, 18,000 and 16,850 cm^{-1}, which were also visible for Zr/Si-6Al and, to a lesser extent, Zr/Si-9Al. These bands must, therefore, be ascribed to a metallocene species that can be formed without MAO. For inspiration we turned to the simplest zirconium chloride compound, namely $ZrCl_4$ (Structure **15**). The simulated UV–vis spectrum of the monomeric $ZrCl_4$ indicates that the lowest absorption energy is 46,650 cm^{-1}, as illustrated in Figure S4b in the Supporting Information. In practice, $ZrCl_4$ adopts a polymeric structure in which each octahedral zirconium center shares four chloride ligands with neighboring zirconium centers, forming the backbone, and has two chloride ligands in the side chain, as indicated in Figure S6. The experimental spectrum in Figure S6, indeed indicates that $ZrCl_4$ also shows three bands at 21450, 17150, and 16,100 cm^{-1}, ascribed to large distance charge transfer excitations. We propose that

the metallocene dichloride precursor can adopt a similar structure with the two cyclopentadienyl ligands in the side chain and the chloride ligands shared in the backbone with neighboring metallocenes (Structure **A**). These species are formed in the absence of large amounts of $AlMe_2^+$. In parallel, we propose that the formed structure **8** can lose the $AlMe_2^+$ and adopt a polymeric structure with methyl ligands in the chain and the same cyclopentadienyl ligands in the side chain (Structure **B**). The band at 20,400 cm^{-1} is then ascribed to this species and its increasing contribution correlates with the increasing MAO loading, as illustrated in Fig. 4 and Table 1. It would be an interesting topic for future studies to further investigate and confirm the presence of such polymeric metallocene species using, for instance, EXAFS measurements. Furthermore, based on the results in this work, it remains unclear whether such polymeric species can become active in the olefin polymerization reaction, which could be a second interesting topic for future studies.

4. Conclusions

An extensive combined UV–vis/TD–DFT characterization study of five silica-supported metallocene-based olefin polymerization catalysts with increasing MAO co-catalyst loading revealed the main activation mechanism of the metallocene precursor by MAO, as shown in Scheme 2. The dichloride metallocene precursor is activated through the interaction with $AlMe_2^+$ species inherent to the solid MAO activator. The precursor in complex with $AlMe_2^+$ exchanges ligands with the MAO, replacing the chloride ligands with methyl groups. Upon the release of TMA, the cationic monomethylated metallocene species is generated, which is assumed to be the active species in the olefin polymerization reaction. This species, however, is not stable on the surface and either remains present in the $AlMe_2^+$ stabilized form, or adopts a polymeric structure. It is proposed that during olefin polymerization, the insertion of the olefin monomers induces the release of TMA in the former case or induces the polymeric structure to break up in monomeric metallocenes in the latter case.

In the case of a low amount of MAO, the metallocene precursor can become deactivated through the interaction with remaining silanol groups on the surface. If there are not enough $AlMe_2^+$ species, this can also induce the metallocene precursor to adopt a polymeric form. All results are in accordance with previous work on the important role of $AlMe_2^+$ species in solid activators for single-site olefin polymerization catalysts [47,48]. Importantly, with increasing MAO loading, the catalysts are more active in the olefin polymerization reaction. This is correlated with the observation of more $AlMe_2^+$–bound metallocenes with a shift towards the methylated form (structure **8**) at the expense of the chloride form (structure **6**) and it is associated with an increase of the adopted polymeric structure of the active cationic monomethylated metallocene.

Acknowledgements

The authors thank Albemarle and the Netherlands Organization for Scientific Research (NWO) (Vidi 723.012.104) for financial support. Katarina Stanciakova (Utrecht University) is acknowledged for her support and insight in performing the calculations.

Appendix A. Supplementary data

Supplementary data associated with this article can be found, in the online version, at https://doi.org/10.1016/j.cattod.2018.11.019.

References

[1] J. P. Hogan, R. L. Banks, US2825721, 1958.
[2] M.P. McDaniel, Adv. Catal. 53 (2010) 123–606.
[3] B.M. Weckhuysen, I.E. Wachs, R.A. Schoonheydt, Chem. Rev. 96 (1996) 3327–3349.
[4] E. Groppo, C. Lamberti, S. Bordiga, G. Spoto, A. Zecchina, Chem. Rev. 105 (2005) 115–183.
[5] K. Ziegler, Rubber Chem. Technol. 38 (1963) 23–36.
[6] J.A. Ewen, Stud. Surf. Sci. Catal. 25 (1986) 271–292.
[7] M. Bochmann, Curr. Opin. Solid State Mater. Sci. 2 (1997) 639–646.
[8] M. Bochmann, G.J. Pindado, S.J. Lancaster, J. Mol. Catal. A Chem. 146 (1999) 179–190.
[9] M. Linnolahti, J.R. Severn, T.A. Pakkanen, Angew. Chem. Int. Ed. 47 (2008) 9279–9283.
[10] G. Fink, B. Steinmetz, J. Zechlin, C. Przybyla, B. Tesche, Chem. Rev. 100 (2000) 1377–1390.
[11] J.R. Severn, J.C. Chadwick, R. Duchateau, N. Friederichs, Chem. Rev. 105 (2005) 4073–4147.
[12] H. Sinn, W. Kaminsky, H.-J. Vollmer, R. Woldt, Angew. Chem. Int. Ed. 19 (1980) 390–392.
[13] W. Kaminsky, Catal. Today 20 (1994) 257–271.
[14] W. Kaminsky, J. Polym. Sci. Part A: Polym. Chem. 42 (2004) 3911–3921.
[15] W. Kaminsky, A. Bark, R. Steiger, J. Mol. Catal. 74 (1992) 109–119.
[16] S. Collins, W.M. Kelly, D.A. Holden, Macromolecules 25 (1992) 1780–1785.
[17] W. Kaminsky, Front. Chem. Sci. Eng. (2018), https://doi.org/10.1007/s11705-018-1715-x.
[18] W. Kaminsky, H. Winkelbach, Top. Catal. 7 (1999) 61–67.
[19] B. Heurtefeu, C. Bouilhac, E. Cloutet, D. Taton, A. Deffieux, H. Cramail, Prog. Polym. Sci. 36 (2011) 89–126.
[20] F. Ciardelli, a. Altomare, M. Michelotti, Catal. Today 41 (1998) 149–157.
[21] M. Bochmann, Organometallics 29 (2010) 4711–4740.
[22] E.Y.X. Chen, T.J. Marks, Chem. Rev. 100 (2000) 1391–1434.
[23] H.S. Zijlstra, S. Harder, Eur. J. Inorg. Chem. 2015 (2015) 19–43.
[24] E. Zurek, T. Ziegler, Prog. Polym. Sci. 29 (2004) 107–148.
[25] M. Linnolahti, S. Collins, ChemPhysChem 18 (2017) 3369–3374.
[26] L. Luo, S. A. Sangokoya, X. Wu, S. P. Diefenbach, B. Kneale, US8354485B2, 2013.
[27] T.K. Trefz, M.A. Henderson, M.Y. Wang, S. Collins, J.S. McIndoe, Organometallics 32 (2013) 3149–3152.
[28] F. Ghiotto, C. Pateraki, J. Tanskanen, J.R. Severn, N. Luehmann, A. Kusmin, J. Stellbrink, M. Linnolahti, M. Bochmann, Organometallics 32 (2013) 3354–3362.
[29] J.T. Hirvi, M. Bochmann, J.R. Severn, M. Linnolahti, ChemPhysChem 15 (2014) 2732–2742.
[30] M.S. Kuklin, J.T. Hirvi, M. Bochmann, M. Linnolahti, Organometallics 34 (2015) 3586–3597.
[31] E.P. Talsi, N.V. Semikolenova, V.N. Panchenko, A.P. Sobolev, D.E. Babushkin, aa. Shubin, V.A. Zakharov, J. Mol. Catal. A Chem. 139 (1999) 131–137.
[32] G.W. Coates, Chem. Rev. 100 (2000) 1223–1252.
[33] M. Bochmann, J. Organomet. Chem. 689 (2004) 3982–3998.
[34] D.E. Babushkin, N.V. Semikolenova, V.A. Zakharov, E.P. Talsi, Macromol. Chem. Phys. 201 (2000) 558–567.
[35] K.P. Bryliakov, N.V. Semikolenova, D.V. Yudaev, V.A. Zakharov, H.H. Brintzinger, M. Ystenes, E. Rytter, E.P. Talsi, J. Organomet. Chem. 683 (2003) 92–102.
[36] T.K. Trefz, M.a. Henderson, M. Linnolahti, S. Collins, J.S. McIndoe, J. Scott McIndoe, Chem. - A Eur. J. 21 (2015) 2980–2991.
[37] D. Coevoet, H. Cramail, A. Deffieux, Macromol. Chem. Phys. 867 (1996) 855–867.
[38] D. Coevoet, H. Cramail, A. Deffieux, Macromol. Chem. Phys. 199 (1998) 1451–1457.
[39] J.-N. Pédeutour, D. Coevoet, H. Cramail, A. Deffieux, Macromol. Chem. Phys. 1221 (1999) 1215–1221.
[40] D. Coevoet, H. Cramail, A. Deffieux, C. Mladenov, J.-N. Pédeutour, F. Peruch, Polym. Int. 263 (1999) 257–263.
[41] H.S. Zijlstra, M. Linnolahti, S. Collins, J.S. Mcindoe, Organometallics 36 (2017) 1803–1809.
[42] M.C. Haag, C. Krug, J. Dupont, G.B. De Galland, J.H.Z. Dos Santos, T. Uozumi, T. Sano, K. Soga, J. Mol. Catal. A Chem. 169 (2001) 275–287.
[43] N. L. Krzystowczyk, S. P. Diefenbach, E. A. Burt, US005739368A, 1998.
[44] D. Bianchini, J.H.Z. Dos Santos, T. Uozumi, T. Sano, J. Mol. Catal. A Chem. 185 (2002) 223–235.
[45] T. Sano, H. Hagimoto, S. Sumiya, Y. Naito, Y. Oumi, T. Uozumi, K. Soga, Microporous Mesoporous Mater. 44–45 (2001) 557–564.
[46] V. Busico, R. Cipullo, R. Pellecchia, G. Talarico, A. Razavi, Macromolecules 42 (2009) 1789–1791.
[47] M.E.Z. Velthoen, H. Meeldijk, F. Meirer, B.M. Weckhuysen, Chem. - A Eur. J. 24 (2018) 11944–11953.
[48] M.E.Z. Velthoen, A. Muñoz-Murillo, A. Bouhmadi, M. Cecius, S. Diefenbach, B.M. Weckhuysen, Macromolecules 51 (2018) 343–355.
[49] M. Wojdyr, J. Appl. Crystallogr. 43 (2010) 1126–1128.
[50] ADF2014.06, n.d., SCM, Theoretical Chemistry, the Vrije Universiteit.
[51] G. te Velde, F.M. Bickelhaupt, E.J. Baerends, C. Fonseca Guerra, S.J.A. van Gisbergen, J.G. Snijders, T. Ziegler, J. Comput. Chem. 22 (2001) 931–967.
[52] T. Yanai, D.P. Tew, N.C. Handy, Chem. Phys. Lett. 393 (2004) 51–57.
[53] M. Seth, T. Ziegler, J. Chem. Theory Comput. 8 (2012) 901–907.
[54] E. Van Lenthe, E.J. Baerends, J. Comput. Chem. 24 (2003) 1142–1156.
[55] S.J.A. van Gisbergen, J.G. Snijders, E.J. Baerends, Comput. Phys. Commun. 118 (1999) 119–138.
[56] M.J.G. Peach, P. Benfield, T. Helgaker, D.J. Tozer, J. Chem. Phys. 128 (2008) 044118.
[57] N.I. Mäkelä, H.R. Knuuttila, M. Linnolahti, T.A. Pakkanen, M.A. Leskelä, Macromolecules 35 (2002) 3395–3401.
[58] B.L. Moroz, N.V. Semikolenova, A.V. Nosov, V.A. Zakharov, S. Nagy, N.J. O'Reilly, J. Mol. Catal. A Chem. 130 (1998) 121–129.
[59] O.Y. Lyakin, K.P. Bryliakov, V.N. Panchenko, N.V. Semikolenova, V.A. Zakharov, E.P. Talsi, Macromol. Chem. Phys. 208 (2007) 1168–1175.